LETTERS
PUBLISHED ONLINE: 24 NOVEMBER 2014 | DOI: 10.1038/NMAT4143
nature materials

Ultrahigh mobility and giant magnetoresistance in the Dirac semimetal Cd_3As_2

Tian Liang[1], Quinn Gibson[2], Mazhar N. Ali[2], Minhao Liu[1], R. J. Cava[2] and N. P. Ong[1]*

Dirac and Weyl semimetals are 3D analogues of graphene in which crystalline symmetry protects the nodes against gap formation[1–3]. Na_3Bi and Cd_3As_2 were predicted to be Dirac semimetals[4,5], and recently confirmed to be so by photoemission experiments[6–8]. Several novel transport properties in a magnetic field have been proposed for Dirac semimetals[2,9–11]. Here, we report a property of Cd_3As_2 that was unpredicted, namely a remarkable protection mechanism that strongly suppresses backscattering in zero magnetic field. In single crystals, the protection results in ultrahigh mobility, 9×10^6 cm^2 V^{-1} s^{-1} at 5 K. Suppression of backscattering results in a transport lifetime 10^4 times longer than the quantum lifetime. The lifting of this protection by the applied magnetic field leads to a very large magnetoresistance. We discuss how this may relate to changes to the Fermi surface induced by the applied magnetic field.

In a 3D Dirac semimetal, the node at zero energy is protected against gap formation by crystalline symmetry[1–3]. Predictions[4,5] that Cd_3As_2 and Na_3Bi are Dirac semimetals have recently been confirmed by angle-resolved photoemission[6–8]. When time-reversal symmetry (TRS) is broken, the Dirac semimetal is expected to evolve to a Weyl semimetal. This has stimulated intense interest in the possibility of observing 'charge-pumping' effects in the Weyl state[2,9–11]. Here we report an unpredicted transport property. Below 5 K in zero magnetic field, Cd_3As_2 exhibits ultrahigh mobility (9×10^6 cm^2 V^{-1} s^{-1}). The pronounced suppression of the high residual conductivity in a magnetic field H implies that the carriers are protected against backscattering by an unknown mechanism.

Crystals of Cd_3As_2, grown by a flux technique (Supplementary Information) are needle-like with well-defined facets. The longest axis lies along $[1\bar{1}0]$ and the largest face is normal to [112]. In addition to these 'Set A' samples, we also investigated multidomain samples which lack defined facets (Set B). Cd_3As_2 is unusual in that exactly 1/4 of the 64 Cd sites in each unit cell are vacant in the ideal lattice[12]. We have found that a rich spectrum of transport properties exists even among crystals extracted from the same boule. The residual resistivity and mobility (at 5 K) can vary by a factor of 200 (Table 1). A remarkable pattern reflecting this variation is already apparent in Fig. 1a, which plots the x-axis resistivity ρ_1 versus temperature T (we take $\hat{\mathbf{x}} \parallel [1\bar{1}0]$ and $\hat{\mathbf{z}} \parallel [112]$; subscripts 1 and 2 refer to axes x and y, respectively). Above 50 K, the resistivity profiles in Set A samples are similar. However, as T decreases from 50 to 5 K, ρ_1 falls steeply, implying a strong enhancement in the transport lifetime τ_{tr}. In A5, the enhancement results in a residual resistivity ratio (RRR) of 4,100 and a residual resistivity considerably lower than that in high-purity Bi (refs 13,14; 21 versus 100 nΩ cm). By contrast, this enhancement is completely absent in samples B1 and B7. A first clue to the enhancement in τ_{tr} comes from examining the resistivity anisotropy $\gamma(T) = \rho_2/\rho_1$. Using the Montgomery technique[15], we have determined that $\gamma(T)$ increases monotonically with decreasing T. As shown in Fig. 1b, $\gamma(T)$ at 5 K rises to 20–30 in samples with large lifetime enhancements (A1 and A5), whereas γ is only 2.7 in A4, which has the smallest enhancement (Table 1). (To rule out the possibility that the very small ρ_1 results from a thin surface layer of Cd, we have carried out several tests described in the Supplementary Information.)

The results in Fig. 1a,b suggest that, at low T, the carrier mobilities μ_1 and μ_2 become very large, but may be highly anisotropic. Employing the magnetic field as a 'yardstick', we have managed to determine the mobility directly by measuring the resistivity tensor $\rho_{ij}(H)$ to high resolution in the weak-field regime. As discussed below (Fig. 2), curves of $\sigma_{xy}(H)$ are obtained by inverting the matrix ρ_{ij}. In all samples, $\sigma_{xy}(H)$ exhibits the 'dispersive-resonance' profile, with sharp peaks that reflect the elliptical cyclotron orbit executed in weak H. In standard Bloch–Boltzmann transport, the reciprocal of the peak field $1/B_{max}$ equals the geometric mean of the mobilities $\mu_m \equiv \sqrt{\mu_1\mu_2}$. Hence, with $\gamma(T)$ known, we may obtain μ_1 and μ_2. (As a check, we have measured B_{max} of σ_{xy} at several T in one sample (A5). As shown in the Supplementary Information, we find that $\mu_m(T)$ and $\mu_1(T)$ track the steep decrease in σ_1^0 as T increases from 5 to 100 K.)

As shown in Fig. 1c, the curves of $\sigma_{xy}(H)$ at 5 K in A4, A5, A6 and A8 exhibit the dispersion profile described. Remarkably, B_{max} shrinks by a factor of 85 (420 mT to 5 mT) as μ_m increases across the samples. The large variation in μ_1 and μ_m scales well with the residual conductivity σ_1^0 (Fig. 1d). Hence we conclude that the anomalously low residual resistivities arise from mobilities that attain ultrahigh values of 10^7 cm^2 V^{-1} s^{-1}, far higher than in previous studies[16–18]. For comparison, the highest electron mobility in Bi is reported[14] to be 9×10^7 cm^2 V^{-1} s^{-1} (Supplementary Information). The highest mobility observed to date in the two-dimensional electron gas (2DEG) in an AlGaAs/GaAs heterojunction is 3.6×10^7 cm^2 V^{-1} s^{-1} (ref. 19). (Despite the 100-fold change in B_{max}, the curves of $\sigma_{xy}(H)$ in the four samples collapse to the same curve when plotted in scaled variables (Supplementary Fig. 6). In Supplementary Section 3, we describe how the scaling excludes the scenario of a highly disordered system with a broad distribution of lifetimes.)

We turn next to the giant MR observed in all samples. Figure 2 shows the curves of $\rho_{ij}(H)$ in A4 and A5, along with curves of $\sigma_{ij}(H) = [\rho_{ij}]^{-1}$ obtained by matrix inversion (similar plots for A6 and A8 are in the Supplementary Information). In a transverse field ($\mathbf{H} \parallel \hat{\mathbf{z}}$), the needle crystal with the lowest mobility A4 ($\mu_1 = 4.0 \times 10^4$ cm^2 V^{-1} s^{-1}) shows a striking H-linear MR

[1]Department of Physics, Princeton University, Princeton, New Jersey 08544, USA. [2]Department of Chemistry, Princeton University, Princeton, New Jersey 08544, USA. *e-mail: npo@princeton.edu

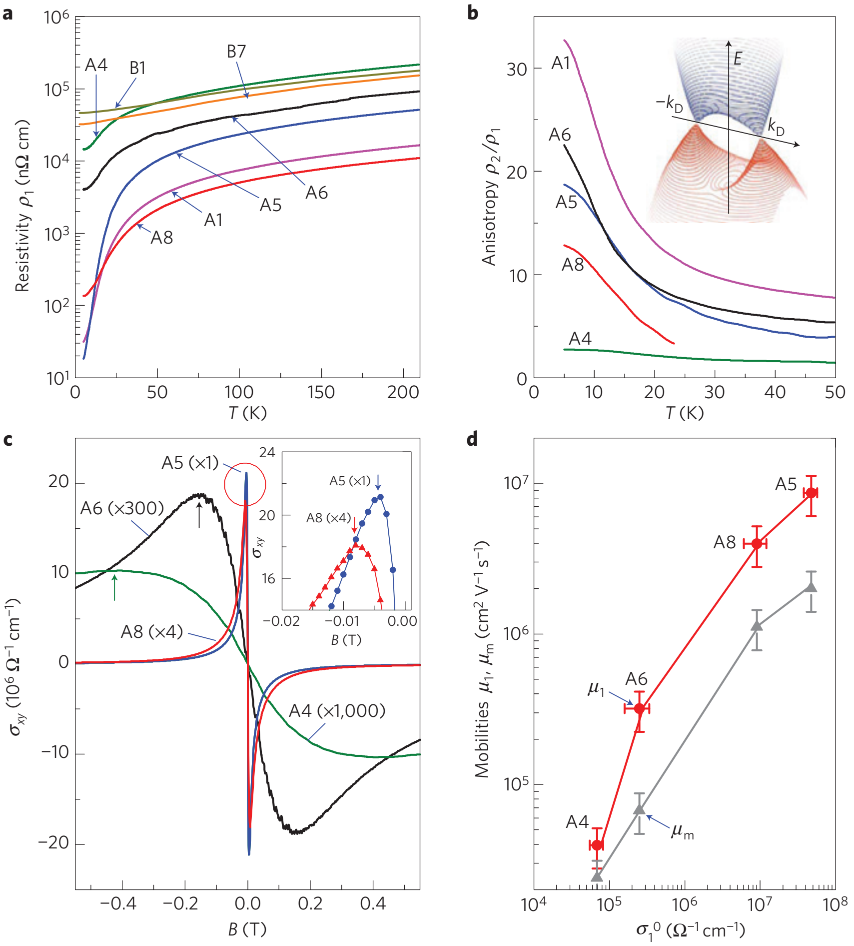

Figure 1 | Transport measurements in a series of Cd_3As_2 samples. **a**, Curves of the resistivity ρ_1 versus T measured along the needle axis $\hat{\mathbf{x}}$ in five Set A and two Set B samples (semilog scale). In needle-shaped crystals (Set A), ρ_1 undergoes a steep decrease below 50 K that is strongly sample dependent. In A5, ρ_1 falls by three orders of magnitude to 21 nΩ cm at 5 K. In A4, however, ρ_1 has a milder decrease (to 14.6 μΩ cm at 5 K). By contrast, the multidomain samples B1 and B7 do not exhibit the steep decrease below 50 K. **b**, Anisotropy $\gamma \equiv \rho_2/\rho_1$ at 5 K, which is large (20–30) in A1 and A5, but modest for A4 (2.7). The inset is a sketch of the energy dispersion $E(k)$ near the Dirac nodes (adapted from ref. 20). **c**, Hall conductivity σ_{xy} versus B in A4, A5, A6 and A8 ($B = \mu_0 H$, with μ_0 the vacuum permeability). The peak locates the geometric-mean mobility $\mu_m \equiv \sqrt{\mu_1 \mu_2}$. For clarity, the region encircled by the red circle is shown expanded in the inset. **d**, Measured mobility μ_m (solid triangles) and x-axis mobility $\mu_1 = \mu_m\sqrt{\gamma}$ (solid circles) versus the zero-H conductivity σ_1^0 for A4, A5, A6 and A8. The error bars are standard errors of the mean.

Table 1 | Parameters of the seven samples investigated.

Sample	ρ_1 (nΩ cm)	γ	RRR	μ_1 (cm^2 V^{-1} s^{-1})	MR (9 T)	n_H (9 T) (10^{18} cm^{-3})
A1	32	32.7	781	$\sim 3\times10^{6*}$	582	9.1
A4	14,600	2.72	21.4	40×10^3	34.5	4.4
A5	21	18.7	4,100	8.7×10^6	1,336	7.4
A6	4,000	22.6	32.2	320×10^3	112	12.0
A8	110	12.8	118	4.0×10^6	404	13.3
B1	46,500	-	5.37	$\sim 10\times10^{3*}$	36.9	-
B7	32,200	-	7.26	$\sim 20\times10^{3*}$	62.2	15

ρ_1 is the resistivity along $\hat{\mathbf{x}}$ at 5 K. The anisotropy γ is ρ_2/ρ_1 at 5 K (γ is undefined in B1 and B7). RRR is the ratio $\rho_1(300)/\rho_1(5)$. The mobilities are determined from σ_{xy} and γ, except in A1, B1 and B7 (*) where they are estimated from the residual resistivity. MR is the ratio $\rho_{xx}(9\,\mathrm{T})/\rho_{xx}(0)$ at 5 K. The Hall density n_H (9 T) equals $B/e\rho_{yx}$ measured at 9 T (all n-type).

profile (Fig. 2a). All Set B samples also exhibit the H-linear MR (Supplementary Information). From the Hall resistivity ρ_{yx} at large H, we obtain an n-type 'Hall density' $n_H = B/e\rho_{yx} \sim 4.4\times10^{18}$ cm^{-3} at 9 T (Table 1). In A5, with the highest μ_1 (Fig. 2c), the MR is significantly larger, but now has the form H^α, with $\alpha = 2$–2.5 above $\sim$2 T (the trend from H-linear to H^α with increasing μ_1 is robust).

Measurements of the MR and Shubnikov–de Haas (SdH) oscillations in a tilted field $\mathbf{H}$ provide further insight on the enhanced lifetime (we fix $\mathbf{H}$ in the x–z plane at an angle θ to $\hat{\mathbf{x}}$). The MR in A1 at 2.5 K is shown in Fig. 3a,b for several tilt angles θ. (The MR ratio is defined as $\rho_{xx}(T,H)/\rho_1(T,0)$; see Table 1.) A log–log plot of the MR in A1 is plotted in the inset of Fig. 3a. As $\mathbf{H}$ is tilted towards $\hat{\mathbf{x}}$ ($\theta \to 0$), the MR decreases rapidly. In Fig. 3c,d we show the MR in Sample B7, which has a similar variation versus θ.

To highlight the SdH oscillations, we plot traces of ρ_{xx} in A1 for $\theta = 6°$, 9° and 12° in Fig. 4a. In sharp contrast to the MR, varying θ has very little effect on the cross-section S_F of the Fermi surface (FS) inferred from the SdH period in all samples. The weak variation of S_F with θ (inset) implies a nearly spherical FS and isotropic v_F, in good agreement with earlier experiments[16,18]. This contrasts with the strong anisotropy γ shown in Fig. 1b (see below). Band calculations[5] and a recent STM study[20] reveal Dirac nodes at $(0,0,\pm k_D)$ with $k_D \sim 0.032$ Å^{-1}, and the Fermi energy E_F lying in the conduction band (inset, Fig. 1b). At each θ, the SdH oscillations in both A1 and B7 fit very closely to the Lifshitz–Kosevich expression with a single frequency (Fig. 4a and Supplementary Information,

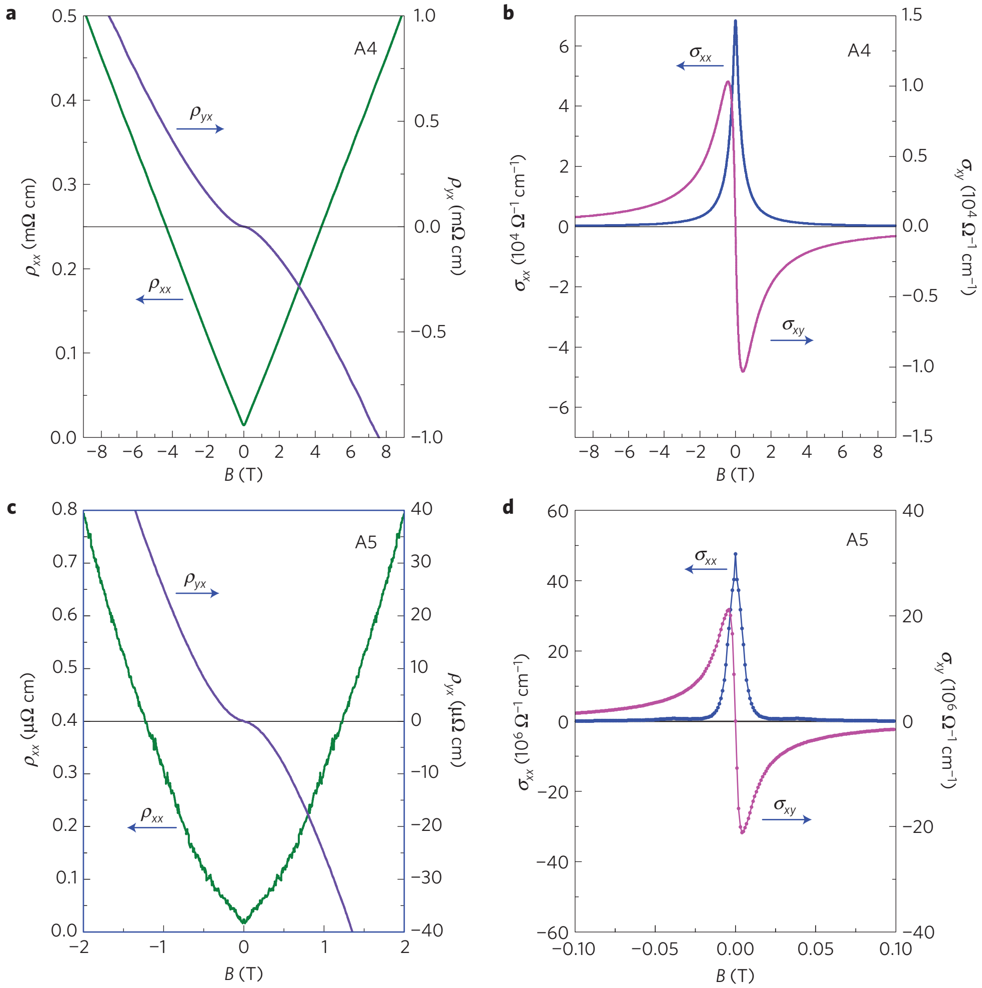

Figure 2 | Conversion of the resistivity matrix ρ_{ij} to the conductivity matrix σ_{ij}. **a**, Resistivity ρ_{xx} for Sample A4, exhibiting an unusual H-linear profile, and Hall resistivity ρ_{yx} (n-type in sign), showing a slight anomaly in weak H (measured at 5 K with $\mathbf{H} \parallel \hat{\mathbf{z}}$ and current $\mathbf{I} \parallel \hat{\mathbf{x}}$; $B = \mu_0 H$). **b**, Inferred conductivity $\sigma_{xx}(H)$ and Hall conductivity $\sigma_{xy}(H)$ for Sample A4. The sharp extrema in σ_{xy} at ±0.42 T locate the geometric-mean mobility $\mu_m = \sqrt{\mu_1 \mu_2}$. **c**, ρ_{xx} and ρ_{yx} at 5 K in Sample A5. **d**, Corresponding curves of $\sigma_{ij}(H)$ for Sample A5. The peaks in σ_{xy} now occur at ±5.0 mT, reflecting the much higher μ_m in A5 (by a factor of 85). In A5, the MR is also larger, but becomes H^2 at large fields. Curves for samples A6 and A8 are shown in the Supplementary Information. Typical dimensions of the crystals are 1.5 × 0.3 × 0.2 mm^3 (see Supplementary Table 1 for exact dimensions).

respectively). In addition to S_F, the fits yield a high Fermi velocity $v_F = 9.3 \times 10^5$ m s^{-1} and a Fermi energy $E_F = 232$ mV, consistent with recent STM (ref. 20) and ARPES experiments[6–8]. The electron density $n = k_F^3/3\pi^2 \simeq 1.9 \times 10^{18}$ cm^{-3} is a factor of two to ten smaller than n_H (Table 1). Tracking the SdH signal to 45 T, we reach the $N = 1$ Landau level (LL) at 27 T and begin accessing the $N = 0$ LL above 36 T (Supplementary Fig. 8). As discussed in Supplementary Section 4, the presence of a second band can be excluded to a resolution of 3% of the main SdH amplitude. Surprisingly, the quantum lifetime is found to be very short ($\tau_Q = 3$–8.6×10^{-14} s) compared with τ_{tr} derived from μ_1.

For a band with Dirac dispersion, the mobility is expressed as $\mu = e v_F \tau_{tr}/\hbar k_F$. Using k_F and μ_1 (Fig. 1d), we estimate $\tau_{tr} \sim 2.1 \times 10^{-10}$ s in A5, corresponding to a 'transport' mean free path $\ell_{tr} \sim 200$ μm. Defining $R_\tau \equiv \tau_{tr}/\tau_Q$, we find that R_τ attains values 10^4 at 2.5 K. The large R_τ provides an important insight into the anomalously low resistivity. τ_{tr} measures ($2k_F$) backscattering processes that relax the current, whereas τ_Q is sensitive to all processes that cause Landau level (LL) broadening, including forward scattering. Hence R_τ generally exceeds 1. Still, R_τ here is exceptionally large compared with values (10–100) reported for GaAs-based 2DEG (refs 21–23).

The picture that emerges is that, in zero field, there exists a novel mechanism that strongly protects the carriers moving parallel to $\hat{\mathbf{x}}$ against backscattering, despite lattice disorder. In the case of the 2DEG in GaAs/AlGaAs, the large R_τ arises because the dopants are confined to a δ-layer set back from the 2DEG (refs 21–23). Charge fluctuations in the dopant layer lead only to small-angle scatterings, which strongly limit τ_Q but hardly affect τ_{tr}. Here there is no obvious separation of the scattering centres from the conduction electrons, yet R_τ is even larger. As evident in Figs 1 and 3, the protection exists in zero H, but is rapidly removed by a field. Because the FS is nearly isotropic in Cd_3As_2, the full anisotropy γ comes from an anisotropic transport scattering rate $\Gamma_{tr} = 1/\tau_{tr}$. Moreover, as the anisotropy is rapidly suppressed above ~20 K (Fig. 1b), the protection extends only to elastic scattering. It is interesting to contrast our results with ballistic propagation in carbon nanotubes. In nanotubes, the carriers can propagate between contact reservoirs without suffering any elastic collision. In our samples A1 and A5, the Dirac electrons at 5 K undergo a great number of collisions (predominantly forward scattering), leading to severe broadening of the LL; but it takes 10^4 collisions to reverse the momentum. Hence $\ell_{tr} \gg \ell_0$ (the mean free path between collisions).

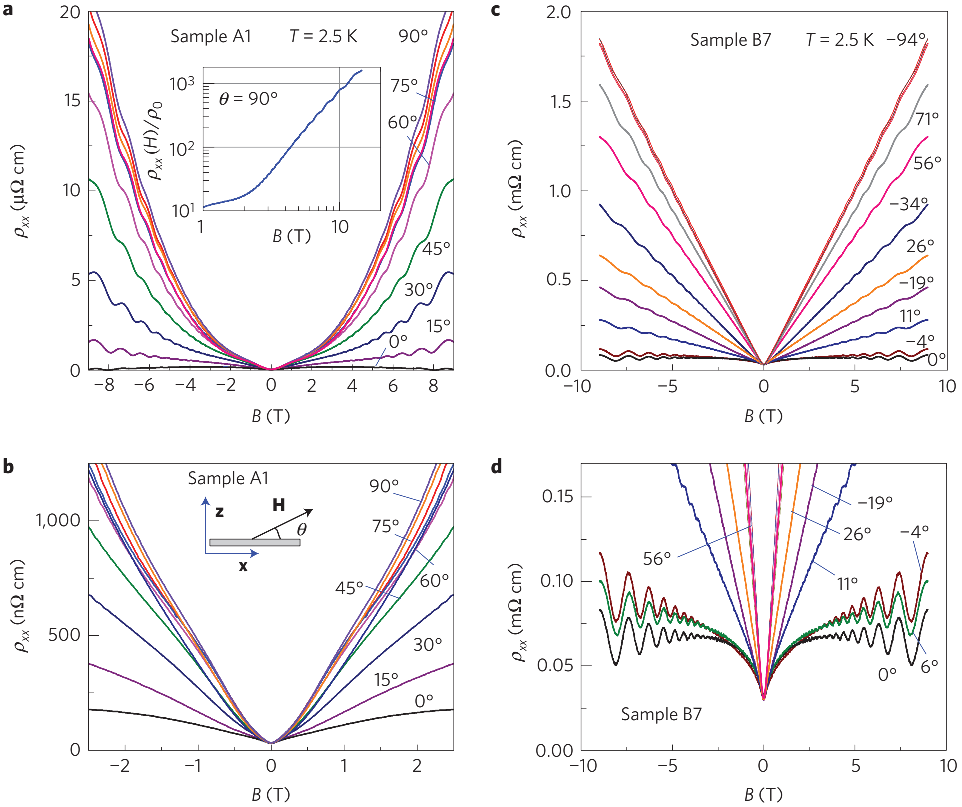

Figure 3 | Magnetoresistance curves $\rho_{xx}(H,\theta)$ and SdH oscillations in tilted H in Cd_3As_2 at 2.5 K in Samples A1 and B7. **a**, MR curves for the high-mobility single crystal A1 plotted for $0<\theta<90°$. The log–log plot in the inset shows that, at 2 T, $\rho_{xx}(H)/\rho_0$ changes from an H-linear increase to an anomalous power law $H^{2.55}$, reaching a value of 1,600 at 15 T ($\theta=90°$). SdH oscillations are resolved at all θ. **b**, In weak H the MR is nearly H-linear. As $\theta\to 0$, the MR rapidly decreases (at fixed H). It acquires a negative contribution for $|\theta|<5°$. **c**,**d**, The multidomain sample B7 exhibits a similar behaviour, except that the striking H-linear dependence persists to 9 T. The tilt angle θ and the x- and z-axes are defined in the inset to **b** [$\hat{\mathbf{z}}\parallel$[112]].

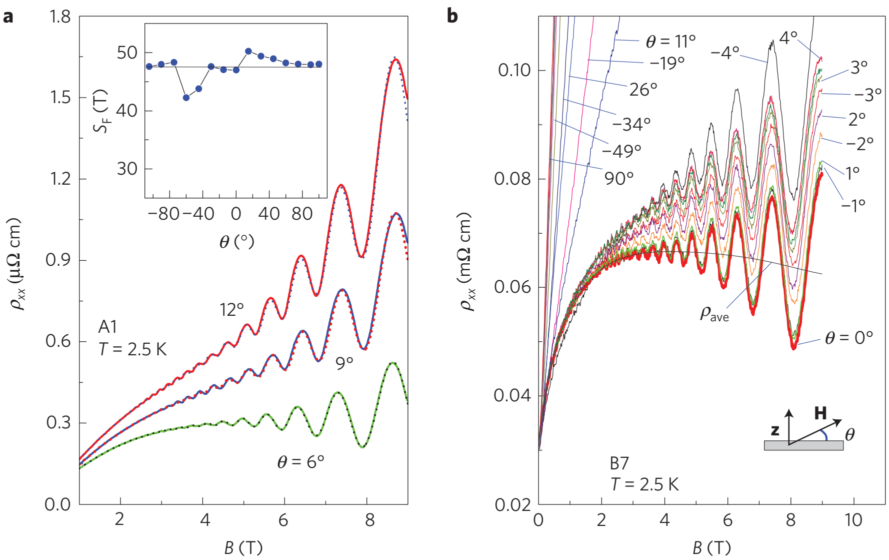

Figure 4 | Shubnikov–de Haas (SdH) oscillations in Samples A1 and B7 at 2.5 K. **a**, SdH oscillations in ρ_{xx} (solid curves), for tilt angles $\theta=6°$, 9° and 12°. Fits to the Lifshitz–Kosevich expression (shown as dotted curves) yield a quantum lifetime $\tau_Q\sim 10^4\times$ times shorter than τ_{tr}. The inset plots the variation of $S_F(\theta)$ about the average 47.5 T. **b**, Traces of ρ_{xx} versus H as θ is changed in 1° steps through 0° at 2.5 K (Sample B7). The curve at $\theta=0$ has a distinct, negative MR contribution (shown by the averaged plot ρ_{ave}). As $|\theta|$ increases from 1° to 4°, the giant positive MR term rapidly dominates. Below 0.2 T, the MR is positive and nearly isotropic (see Supplementary Information for more information).

The giant MR is universally observed in all samples. We find the striking H-linear MR observed in the low-mobility samples (A4 and all Set B samples) especially interesting. Non-saturating H-linear MR is rare in metals and semimetals. It has been reported in $Ag_{2+\delta}Se$ ($\delta\sim 0.01$; refs 24,25) and Bi_2Te_3 (ref. 26), both topological insulators. Abrikosov has derived an H-linear MR for Dirac electrons occupying the lowest LL (ref. 27). However, the H-linear MR here already exists at very low H. We remark on two notable features of the MR in B7. In the limit $H \to 0$, the MR becomes nearly isotropic (Figs 3d and 4b). This implies that a Zeeman coupling to the spin degrees is important (the g-factor is known to exceed 20). Further, when T is raised to 300 K, the H-linear profile is unchanged, except that the cusp at $H = 0$ becomes progressively rounded by thermal broadening. This robustness suggests that an unconventional mechanism for the H-linear MR. Both points are discussed further in the Supplementary Information.

Our finding of a strongly H-dependent Γ_{tr} is consistent with field-induced changes to the FS. In Dirac semimetals, breaking of TRS by H rearranges the Dirac FS (refs 1,2,4,10,11). The FS either splits into two disjoint Weyl pockets (if H couples to both spin and orbital degrees) or becomes two concentric spheres (if H couples to spin alone; ref. 4). Because these changes are linear in H, it would be interesting to see if they can lead to lifting of the protection mechanism and the giant MR observed.

In Dirac semimetals, there is strong interest in whether the chiral term $(e^3/4\pi^2\hbar^2)\mathbf{E}\cdot\mathbf{H}$ can be detected as a negative contribution to the longitudinal MR ($\mathbf{E} \parallel \mathbf{H}$), with $\mathbf{E}$ the electric field (Supplementary Information; refs 9–11,28,29). Clearly, the giant positive MR has to be carefully considered because it constitutes a θ-dependent 'background' that is much larger than the chiral term (we estimate that, at 1 T, the latter decreases ρ_{xx} by roughly 10^{-2}). Although this seems daunting, we note that the competing terms are of opposite signs and are out-of-phase: the chiral term varies as $-\cos\theta$, whereas the positive MR term varies as $\sin\theta$ (vanishes at $\theta = 0$). In Fig. 4b, we plot the MR curves in B7, stepping θ in 1° steps through 0°. Clearly, ρ_{xx} attains a sharp minimum, which we identify as $\theta = 0$ (bold curve), but swings up when $|\theta|$ exceeds 2°. In the curve at $\theta = 0$, we resolve a weak, but distinct negative MR term (see the averaged curve ρ_{ave}). To compare this negative term with the chiral term in a physically meaningful way, we will need to apply larger H and finer control of θ. These experiments are being pursued. After completion of these experiments, we learnt of the results in refs 30,31.

Received 5 May 2014; accepted 20 October 2014; published online 24 November 2014

References

1. Young, S. M. *et al.* Dirac semimetal in three dimensions. *Phys. Rev. Lett.* **108,** 140405 (2012).
2. Wan, X. G., Turner, A. M., Vishwanath, A. & Savrasov, S. Y. Topological semimetal and Fermi-arc surface states in the electronic structure of pyrochlore iridates. *Phys. Rev. B* **83,** 205101 (2011).
3. Fang, C., Gilbert, M. J., Dai, X. & Bernevig, B. Andrei Multi-Weyl topological semimetals stabilized by point group symmetry. *Phys. Rev. Lett.* **108,** 266802 (2012).
4. Wang, Z. J. *et al.* Dirac semimetal and topological phase transitions in A_3Bi (A = Na, K, Rb). *Phys. Rev. B* **85,** 195320 (2012).
5. Wang, Z. J., Weng, H. M., Wu, Q. S., Dai, X. & Fang, Z. Three-dimensional Dirac semimetal and quantum transport in Cd_3As_2. *Phys. Rev. B* **88,** 125427 (2013).
6. Sergey, B. Experimental realization of a three-dimensional Dirac semimetal. *Phys. Rev. Lett.* **113,** 027603 (2014).
7. Liu, Z. K. *et al.* Discovery of a three-dimensional topological Dirac semimetal, Na_3Bi. *Science* **343,** 864–867 (2014).
8. Neupane, M. *et al.* Observation of a three-dimensional topological Dirac semimetal phase in high-mobility Cd_3As_2. *Nature Commun.* **5,** 3786 (2014).
9. Son, D. T. & Spivak, B. Z. Chiral anomaly and classical negative magnetoresistance of Weyl metals. *Phys. Rev. B* **88,** 104412 (2013).
10. Burkov, A. A., Hook, M. D. & Balents, L. Topological nodal semimetals. *Phys. Rev. B* **84,** 235126 (2011).
11. Hosur, P. & Qi, X. Recent developments in transport phenomena in Weyl semimetals. *C. R. Phys.* **14,** 857–870 (2013).
12. Mazhar, N. *et al.* The crystal and electronic structures of Cd_3As_2, the three-dimensional electronic analogue of graphene. *Inorg. Chem.* **53,** 4062–4067 (2014).
13. Mase, S., von Molnar, S. & Lawson, A. W. Galvanomagnetic tensor of bismuth at 20.4° K. *Phys. Rev.* **127,** 1030–1045 (1962).
14. Hartman, R. Temperature dependence of the low-field galvanomagnetic coefficients of bismuth. *Phys. Rev.* **181,** 1070–1086 (1969).
15. Montgomery, H. C. Method for measuring electrical resistivity of anisotropic materials. *J. Appl. Phys.* **42,** 2971–2975 (1971).
16. Rosenman, I. Effet Shubnikov de Haas dans Cd_3As_2: Forme de la surface de Fermi et modele non parabolique de la bande de conduction. *J. Phys. Chem. Solids* **30,** 1385–1402 (1969).
17. Iwami, M., Matsunami, H. & Tanaka, T. Galvanomagnetic effects on single crystals of cadmium arsenide. *J. Phys. Soc. Jpn* **31,** 768–775 (1971).
18. Blom, F. A. P., Neve, J. J. & Nouwens, P. A. M. On the conduction band ansisotropy in semimagnetic semiconducting $(Cd_{1-x}Mn_x)_3As_2$ alloys. *Physica B* **117,** 470–472 (1983).
19. Schlom, D. G. & Pfeiffer, L. N. Upward mobility rocks! *Nature Mater.* **9,** 881–883 (2010).
20. Jeon, S. *et al.* Landau quantization and quasiparticle interference in the three-dimensional Dirac semimetal Cd_3As_2. *Nature Mater.* **13,** 851–856 (2014).
21. Paalanen, M. A., Tsui, D. C. & Hwang, J. C. M. Parabolic magnetoresistance from the interaction effect in a two-dimensional electron-gas. *Phys. Rev. Lett.* **51,** 2226–2229 (1983).
22. Harrang, J. P. *et al.* Quantum and classical mobility determination of the dominant scattering mechanism in the two-dimensional electron-gas of an AlGaAs/GaAs heterojunction. *Phys. Rev. B* **32,** 8126–8135 (1985).
23. Coleridge, P. T. Small-angle scattering in 2-dimensional electron gases. *Phys. Rev. B* **44,** 3793–3801 (1991).
24. Xu, R. *et al.* Large magnetoresistance in non-magnetic silver chalcogenides. *Nature* **390,** 57–60 (1997).
25. Zhang, W. Topological aspect and quantum magnetoresistance of β-Ag_2Te. *Phys. Rev. Lett.* **106,** 156808 (2011).
26. Qu, D. X., Hor, Y. S., Xiong, J., Cava, R. J. & Ong, N. P. Quantum oscillations and Hall anomaly of surface states in the topological insulator Bi_2Te_3. *Science* **329,** 821–824 (2010).
27. Abrikosov, A. A. Quantum magnetoresistance. *Phys. Rev. B* **58,** 2788–2794 (1998).
28. Nielsen, H. B. & Ninomiya, M. The Adler–Bell–Jackiw anomaly and Weyl fermions in a crystal. *Phys. Lett. B* **130,** 389–396 (1983).
29. Parameswaran, S. A., Grover, T., Abanin, D. A., Pesin, D. A. & Vishwanath, A. Probing the chiral anomaly with nonlocal transport in three-dimensional topological semimetals. *Phys. Rev. X* **4,** 031035 (2014).
30. He, L. P. *et al.* Quantum transport evidence for a three-dimensional Dirac semimetal phase in Cd_2As_2. Preprint at http://arXiv.org/abs/1404.2557 (2014).
31. Feng, J. *et al.* Large linear magnetoresitance in Dirac semi-metal Cd_2As_2 with Fermi surfaces close to the Dirac points. Preprint at http://arXiv.org/abs/1405.6611 (2014).

Acknowledgements

We thank A. Bernevig, S. Parameswaran, A. Vishwanath and A. Yazdani for valuable discussions, and N. Yao for assistance with EDX measurements. N.P.O. is supported by the Army Research Office (ARO W911NF-11-1-0379). R.J.C. and N.P.O. are supported by a MURI grant on Topological Insulators (ARO W911NF-12-1-0461) and by the US National Science Foundation (grant number DMR 0819860). T.L. acknowledges scholarship support from the Japan Student Services Organization. Some of the experiments were performed at the National High Magnetic Field Laboratory, which is supported by National Science Foundation Cooperative Agreement No. DMR-1157490, the State of Florida, and the US Department of Energy.

Author contributions

T.L. performed and analysed the measurements. Q.G., M.N.A. and R.J.C. grew the crystals and performed the materials composition and structural analyses. M.L. built a key apparatus. R.J.C. and N.P.O. conceived the project and analysed the results. All authors contributed to preparing the manuscript.

Additional information

Supplementary information is available in the online version of the paper. Reprints and permissions information is available online at www.nature.com/reprints. Correspondence and requests for materials should be addressed to N.P.O.

Competing financial interests

The authors declare no competing financial interests.